Article:
Nohl, J.F., Farr, N.T.H., Sun, Y. et al. (2023) Insights into surface chemistry down to nanoscale: an accessible colour hyperspectral imaging approach for scanning electron microscopy. Materials Today Advances, 19. 100413. ISSN: 2590-0498

https://doi.org/10.1016/j.mtadv.2023.100413

Materials Today Advances 19 (2023) 100413

Contents lists available at ScienceDirect

Materials Today Advances

journal homepage: www.journals.elsevier.com/materials-today-advances/

Insights into surface chemistry down to nanoscale: An accessible colour hyperspectral imaging approach for scanning electron microscopy

James F. Nohl [a,b,*], Nicholas T.H. Farr [a,c], Yige Sun [b,d,e], Gareth M. Hughes [f], Nicola Stehling [a], Jingqiong Zhang [g], Fodio Longman [a,h], Gemma Ives [i], Zuzana Pokorná [j], Filip Mika [j], Vikas Kumar [a,k], Lyudmila Mihaylova [g], Chris Holland [a], Serena A. Cussen [a,b], Cornelia Rodenburg [a]

[a] Department of Materials Science and Engineering, The University of Sheffield, Mappin Street, Sheffield, S1 3JD, UK
[b] The Faraday Institution, Quad One, Becquerel Avenue, Harwell Campus, Didcot, OX11 0RA, UK
[c] Insigneo Institute for in Silico Medicine, Pam Liversidge Building, Sir Robert Hadfield Building, The University of Sheffield, Mappin Street, Sheffield, S1 3JD, UK
[d] Department of Materials, University of Oxford, Parks Road, Oxford, OX1 3PH, UK
[e] Linacre College, University of Oxford, St. Cross Road, Oxford, OX1 3JA, UK
[f] David Cockayne Centre for Electron Microscopy, Department of Materials, University of Oxford, Parks Road, Oxford, OX1 3PH, UK
[g] Department of Automatic Control and Systems Engineering, The University of Sheffield, Amy Johnson Building, Portobello Street, Sheffield, S1 3JD, UK
[h] National Space Research and Development Agency, Obasanjo Space Centre, Umaru Yar'udua Way, PMB 473, Abuja, Nigeria
[i] IT Services, The University of Sheffield, 10-12 Brunswick Street, Sheffield, S10 2FN, UK
[j] Institute of Scientific Instruments of the CAS, Královopolská 147/62, 612 00, Brno-Královo Pole, Czech Republic
[k] Materials Innovation Centre, School of Engineering, University of Leicester, Leicester, LE1 7RH, UK

A B S T R A C T

Chemical imaging (CI) is the spatial identification of molecular chemical composition and is critical to characterising the (in-) homogeneity of functional material surfaces. Nanoscale CI on bulk functional material surfaces is a longstanding challenge in materials science and is addressed here.

We demonstrate the feasibility of surface sensitive CI in the scanning electron microscope (SEM) using colour enriched secondary electron hyperspectral imaging (CSEHI). CSEHI is a new concept in the SEM, where secondary electron emissions in up to three energy ranges are assigned to RGB (red, green, blue) image colour channels. The energy ranges are applied to a hyperspectral image volume which is collected in as little as 50 s. The energy ranges can be defined manually or automatically.

Manual application requires additional information from the user as first explained and demonstrated for a lithium metal anode (LMA) material, followed by manual CSEHI for a range of materials from art history to zoology.

We introduce automated CSEHI, eliminating the need for additional user information, by finding energy ranges using a non-negative matrix factorization (NNMF) based method. Automated CSEHI is evaluated threefold: (1) benchmarking to manual CSEHI on LMA; (2) tracking controlled changes to LMA surfaces; (3) comparing automated CSEHI and manual CI results published in the past to reveal nanostructures in peacock feather and spider silk. Based on the evaluation, CSEHI is well placed to differentiate/track several lithium compounds formed through a solution reaction mechanism on a LMA surface (eg. lithium carbonate, lithium hydroxide and lithium nitride). CSEHI was used to provide insights into the surface chemical distribution on the surface of samples from art history (mineral phases) to zoology (di-sulphide bridge localisation) that are hidden from existing surface analysis techniques. Hence, the CSEHI approach has the potential to impact the way materials are analysed for scientific and industrial purposes.

1. Introduction

Microscopy has been a vital driver of scientific innovation, not least because it caters to humankind's strongest sense: vision. Secondary electron hyperspectral imaging (SEHI) presents an opportunity to reveal and communicate information beyond what is visible in a single grey-scale secondary electron (SE) image. Using SE spectroscopy and SEHI, elemental [1,2], and chemical mapping is possible [3], as well as visualisation of the distribution of properties such as crystallinity, crystal orientation and even functional groups down to the nanoscale [4–8]. However, such information is not easily accessible to most scanning electron microscope (SEM) users due to the absence of reliable SE spectral databases. Here we present colour enriched SEHI (CSEHI) as a method for producing accessible colour images reflecting surface

* Corresponding author. Department of Materials Science and Engineering, The University of Sheffield, Mappin Street, Sheffield, S1 3JD, UK.
E-mail address: jnohl1@sheffield.ac.uk (J.F. Nohl).

https://doi.org/10.1016/j.mtadv.2023.100413
Received 14 June 2023; Received in revised form 27 July 2023; Accepted 28 July 2023
Available online 23 August 2023

chemistry from SE emissions in low-voltage (LV-) SEM.

LV-SEMs developed to meet characterisation requirements of beam sensitive materials with light element components, such as biological [9], catalytic [10], photovoltaic [4] and fusion reactor [11] materials. SEs have an optimal yield in these imaging conditions and are considered key to establishing new techniques and workflows for LV-SEM [12]. However, there are currently limited options for microanalysis in the LV-SEM due to lower yield of backscatter electrons (BSEs) and X-rays when the beam accelerating voltage is less than 5 kV (commonly used as the threshold for LV-SEM) [13,14]. These techniques offer only elemental information via characteristic X-ray lines or Z-contrast (in the case of BSE) and thus chemical information is missing.

In X-ray based elemental mapping (commonly named energy dispersive X-Ray (EDX) mapping), colour is introduced by assigning characteristic X-ray emission energy ranges colour channels. The resulting colour image allows visualisation of elemental distribution in the material [15,16]. In LV-SEM conditions, maximisation of collection of the X-rays generated has been pursued, for example with windowless and high solid angle silicon drift detectors [17]. Nevertheless, X-ray signal generation constraints still exist for light elements such as Li [18] and for many beam sensitive materials [9].

For light elements such as Li and H, the current alternative to X-ray elemental mapping are correlative microscopy approaches. Correlation between the SE image and the elemental distribution obtained by focused ion beam (FIB) techniques: secondary ion mass spectrometry (SIMS) [19] and FIB induced fluorescence spectroscopy (FIB-FS) [20] for instance, or with chemical bonding information by correlative Raman spectroscopy [21] can reveal information about light-element surface chemistry. The combination of the multiple signals creates challenges in interpreting the lateral and depth resolution of composite images, especially since the SE signal comes from <5 nm from the material surface (see simulated SE mean escape depths [22]). Lateral and depth resolution are important considerations in chemical imaging (CI) on the nanoscale as CI is defined as the spatial identification of the molecular chemical composition [23]. SE spectroscopy and SEHI meanwhile have proven sensitive to surface compounds of hydrogen such as amorphous hydrogenated carbon [24,25].

The CSEHI method consists of SEHI data collection (reviewed [26]) combined with colour enrichment as part of the data analysis. CSEHI produces an RGB image reflecting energy information from the SEHI data volume, where pixels in the RGB colour channels are assigned intensity values according to customisable SE emission energy ranges. A manual procedure to determine the energy ranges for CSEHI is explained and demonstrated on the example of CI for lithium metal anode (LMA) surfaces. The additional background information used for this application are models of the valence band density of states (DOS) of likely Li compounds.

As the interpretation of SE spectra is still in its infancy, even for single element materials such as pure metals [1], the choice of energy ranges to produce informative colour images can be daunting, especially for inexperienced users, and in the absence of a SE spectroscopy reference repository. Similar difficulties in optical hyperspectral imaging in industrial applications led to the development of colour-CI - a method that combines the advantages of CI with colour image processing [23]. The goal of colour-CI is to make chemical material properties accessible to a completely new range of users through new approaches to data processing [27]. Following this concept, we develop a method that automates the selection of energy ranges for CSEHI without the need for any additional background information. We show results of CSEHI on a range of complex functional materials from art history to zoology. Consequently, SEHI datasets have the potential to provide a significant benefit in data-driven materials research [28–30], which applies machine-learning, data-mining, and statistical techniques to diverse applications: from battery [31], solar cell [32] and biological [33] materials to art authentication [34] and electron microscopy [35].

In the automated CSEHI workflow, the selection of energy ranges is based on component SE spectra intensities. Three components are separated from the SEHI data volume using the non-negative matrix factorization (NNMF) algorithm [3], [36–39] from which component SE spectra are derived. Then, selection rules determine the energy ranges in which a component SE spectrum is distinctly the most intense. The automated CSEHI method is explained in detail in section 3.3 of this article.

The results of automated CSEHI were evaluated in three ways. For the LMA application, firstly, manual and automated CSEHI results were compared. Secondly, a controlled change to the surface chemistry of the LMA was made in situ using a plasma-FIB (PFIB) column combined with an LV-SEM. Additionally, manual input energy ranges for CSEHI could be found from past studies and compared to the results of automated CSEHI. Automated CSEHI tends to return narrower energy ranges than manual analysis. We provided evidence that the narrower ranges potentially better reflect actual surface chemistry as discussed in the example of LMA.

2. Materials

Materials from the fields of energy, zoology and arts history are test cases for the proposed approaches and methods: LMA, peacock feather and silk, mineral pigments and lastly photovoltaic organic-inorganic hybrid lead halide perovskite material. A detailed description of these materials and their preparation are given in section 2.0 of the supporting information (SI).

3. Methods

3.1. Low-voltage SEM and secondary electron hyperspectral imaging (SEHI)

Two SEMs were used to generate SEHI data volumes: the Thermo Fisher Scientific Helios G4 PFIB CXe and FEI Helios NanoLab G3 UC. The Helios is a dual beam microscope (electron and ion beam) with high-resolution, low-voltage capable field emission SEM and Focused Ion Beam (FIB). The Thermo Scientific Helios G4 PFIB CXe is equipped with a Xe ion plasma sourced FIB. Instrument parameters used for collection are included in the SI (SI Table 1). An electron beam with 1 kV accelerating voltage was used for SE imaging in all cases. The beam current used was 12.5 pA except in the cases of lithium metal (50 pA) and perovskite solar cell (25 pA). No conductive coating, stage bias or beam deceleration was used.

These instruments have column and detector designs which allow energy filtering of secondary electrons and the collection of SEHI data sets through serial acquisition [40,41]. By stepping the voltage on the mirror electrodes of the through lens detector (TLD), a variable low-pass filter is applied. At each mirror voltage step, an image is formed of electrons with energies that pass the low-pass filter. In this way, a SEHI data volume is acquired over an energy range. Automated data pre-processing scripts were used to register images in the data volume and extract useful image metadata (using the pysehi python module, see section 8). The energy calibration – to evaluate the maximum energy of detected SEs at a defined mirror voltage - is performed through stage bias experiments [26,42] and described in section 2.7 of the SI.

3.2. Colour enriched secondary electron hyperspectral imaging (CSEHI) – manual approach

The CSEHI workflow represents information in the energy dimension of the SEHI data volume as colour. This is possible by adding SE emissions in up to three energy ranges to the colour channels of an RGB image. In manual CSEHI, the energy ranges that contribute to the colour image are chosen by the user. The general process is as follows: the SEHI data volume is smoothed using an anisotropic three-dimensional point spread function, to reduce noise. The data volume is differentiated in the

energy dimension, and the user is prompted to define up to three energy ranges in which SE emissions are assigned to each RGB colour channel, which are shown alongside the average spectrum. The energy ranges for each channel may overlap and may also exclude certain energy ranges from inclusion in the colour image.

3.3. Automation of CSEHI

The definition of up to three energy ranges in manual CSEHI is based on prior knowledge of experimental SE spectra from reference materials or theoretical models. However, another approach is to implement an 'explorative' colouring that maximises the information content in the RGB colour image without any prior knowledge of the material. To achieve this, we introduce an automated procedure that involves splitting the spectrum into three components using a machine learning approach, exploring the NNMF method to determine the spectrum distribution of the components [3], [36–39]. Additionally, we aim to maximise the reliable information in the RGB images by avoiding allocation of colours to energy ranges in which multiple runs of the NNMF component analysis indicate a large degree of uncertainty (workflow represented in Fig. 1).

Specifically, we compare the average component loadings from the multiple runs to ensure consistency and control the initialisation issues inherent with the NNMF method [43] (Fig. 1 steps 7–9). In Fig. 1, step 8 we adopt a combination of rules that checks the dominance of the actual component loading values in each energy interval over initialisation related variations, while also considering the component with the highest loading as the initial component to colour. Finally, these points are then used to select the three colour ranges that map to three energy ranges. Where there are less than three distinct material phases, the automatic colouring may identify fewer than three ranges to colour. Where it is expected that there are more than three material phases, the user can increase the number of components, of which only three may be coloured. A detailed explanation of this approach is presented in the SI section 2.10.

The automated CSEHI is designed to make SEHI more accessible to inexperienced users and to gain an insight to complex functional materials for which there is no additional information such DOS models or experimental reference spectra available. Therefore, we test the automated CSEHI framework rigorously, first by benchmarking it to the results obtained from the manual colouring on the LMA example. Second, we exploit the fact that the LV-SEM is combined with a PFIB column thus allowing controlled change to the surface chemistry. Third, by comparing to CSEHI results obtained on materials for which the relevant manual input for energy ranges was published in the past to exclude any user bias.

4. Manual application of CSEHI using prior knowledge

Fig. 2 provides an overview of the application areas in which manual CSEHI has been applied.

4.1. Lithium metal: using knowledge of density of states model for manual CSEHI

4.1.1. Background

To showcase the ability of CSEHI in accessing surface chemistry of materials composed of light elements, we select the LMA (the atomic number of lithium is 3). LMAs pack more lithium ions into a given space and have a higher theoretical specific capacity (3860 $mAhg^{-1}$ [45]) compared to graphite (372 $mAhg^{-1}$ [46]) and are therefore being developed as the anode in lithium metal batteries (LMBs).

During charge and discharge of a LMB, there is a thin layer of compounds (solid-electrolyte interphase (SEI)) that forms between the anode and liquid electrolyte, due to the electrolyte degradation [47]. The formation of the SEI is largely determined by the solid component surface chemistry and electrochemistry and the resulting SEI layer could be beneficial and detrimental to battery performance. For example, it has been reported that uniform lithium hydroxide and lithium nitride passivation layers grown on lithium metal [48] could stabilise the SEI formed, suppress the Li dendrite growth, protect the separator from being penetrated, and thus the battery from short circuit. However, other polyanion compounds, such as lithium carbonate (Li_2CO_3) are proven to be unstable SEI components and contribute to the battery

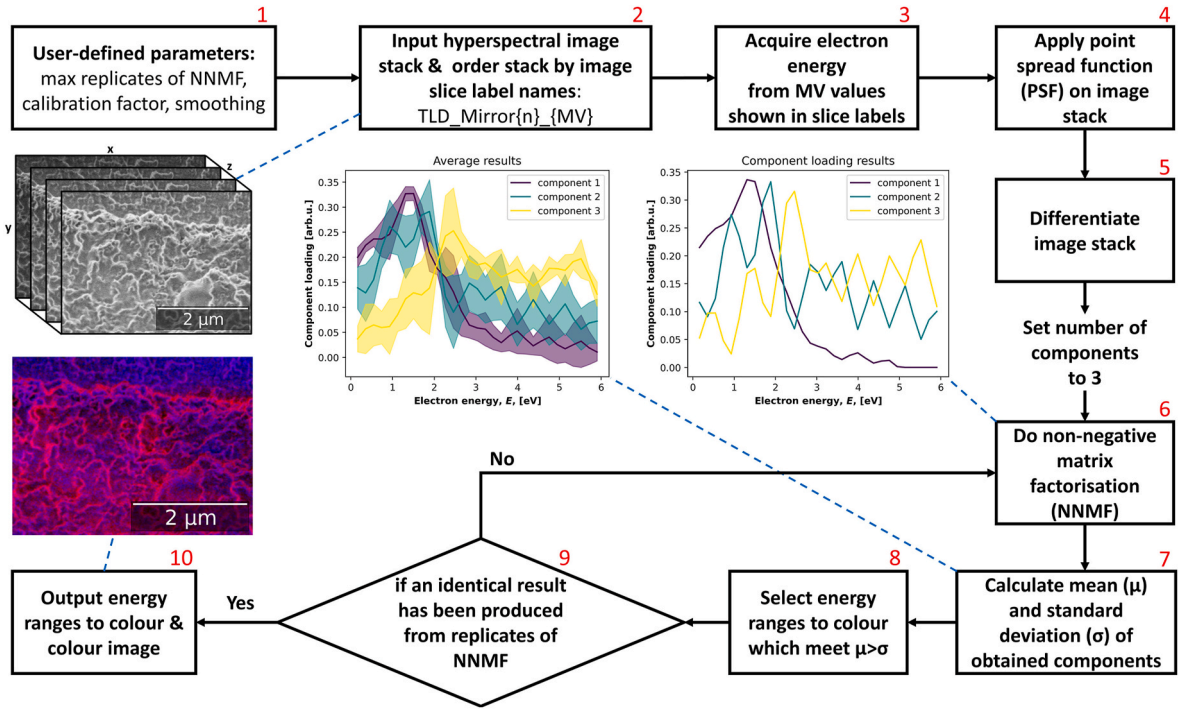

Fig. 1. Flow diagram representation for the automated CSEHI workflow.

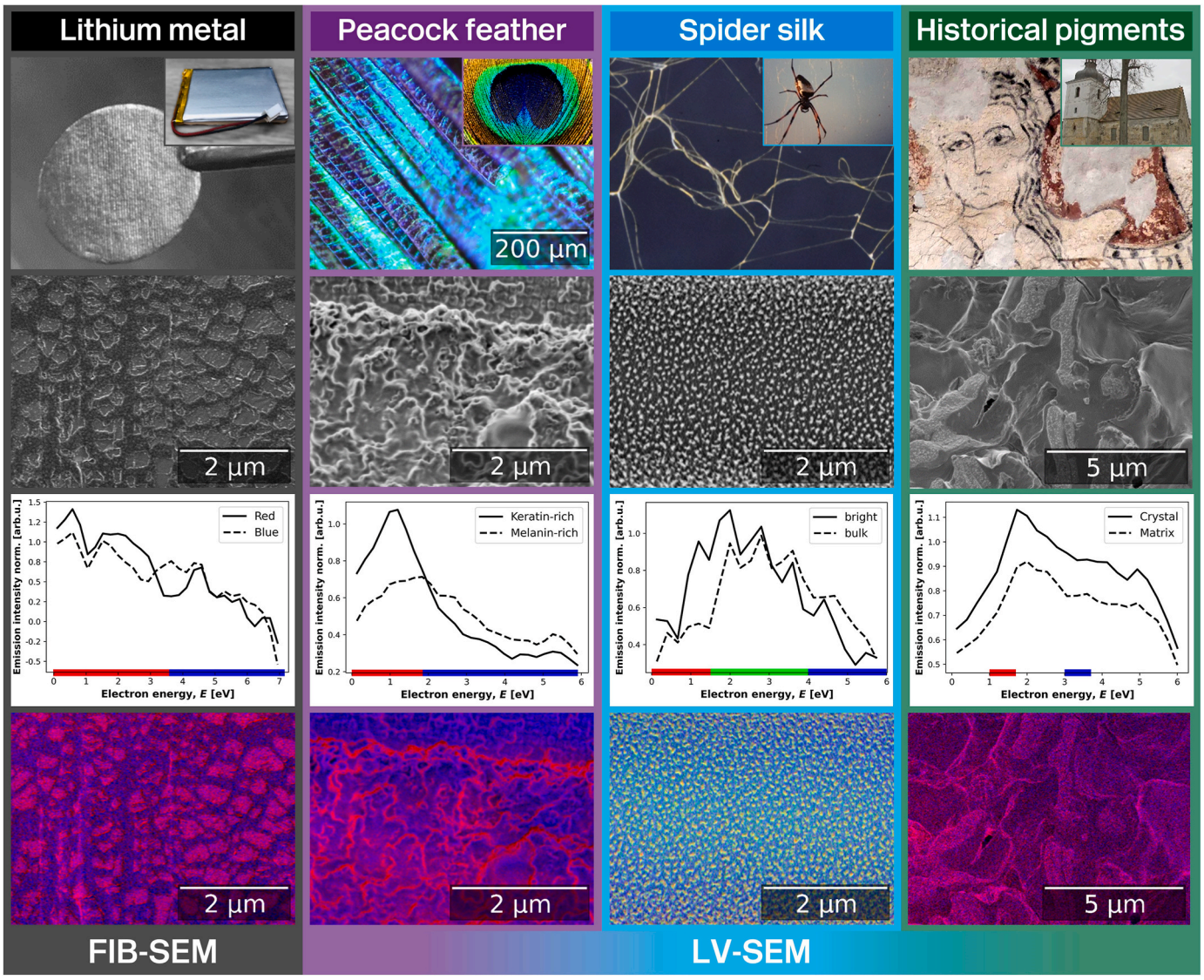

Fig. 2. Application of manual CSEHI to different materials systems. The column titles "Lithium metal", "Peacock feather", "Spider silk" and "Historical pigments" refer to the application area. The second row are images from hyperspectral data volumes and the third row are SEHI derived SE spectra. The colour bars on the SE spectra 'Electron energy, *E*' axis indicate the manual allocation of colour to specific energy ranges based on reference materials or prior knowledge about the materials system. The bottom row shows the resulting CSEHI maps. "Spider silk" inset image reproduced under creative commons license CC0 1.0 (https://creativecommons.org/publicdomain/zero/1.0/deed.en). "Historical pigments" inset reproduced from Hradil et al., "Crocoite $PbCrO_4$ and mimetite $Pb_5(AsO_4)_3Cl$: rare minerals in highly degraded mediaeval murals in Northern Bohemia" [44], with the permission of John Wiley and Sons.

degradation [49]. Therefore, the characterisation and identification these SEI-related Li-compounds, such as lithium hydroxides, lithium nitrides and lithium-carbon compounds, with high spatial and surface depth resolution, is important for gaining insight into the SEI formation mechanism and function.

Since the SEI related Li-compounds and the original LMA surface play a key role in the battery performance, numerous studies have been conducted to characterise and identify with techniques such as nuclear magnetic resonance (NMR) spectroscopy [50], X-ray absorption spectroscopy (XAS) [51], Auger and X-ray photoelectron spectrometry (XPS) [52] and neutron reflectometry [53], and studies include depth stratified analysis of surface chemistry by combined EDX analysis, XPS and time-of-flight secondary ion mass spectrometry (TOF-SIMS) [47]. However, there is a bottleneck in characterisation due to the spatially averaged nature of these surface chemical analyses. SEHI offers the benefit of providing surface chemical information with higher spatial resolution than is available from XPS and Auger electron spectroscopy, without the need for UHV conditions [26].

While SE images are routinely sub-micrometre in resolution, the energy filtering nature of SEHI allows for collection of surface chemical information in conjunction with imaging. Although deconvolution of characteristic SE peaks from the SE spectrum is in its infancy, the reflection of the valence band DOS in SE spectrum fine structure results in characteristic SE spectra from material surfaces [1]. SE spectroscopy can be more sensitive to chemical shift than core level spectroscopies and this effect has been exploited in characterising carbon allotropes [24]. Informed by these studies, we collect and interpret SE spectra from functional material surfaces with complex surface chemistries such as a Li metal exposed to a glovebox environment and subsequent transfer step to the microscope. Here we demonstrate CI using CSEHI to study such lithium compound rich surfaces and compare the 'as-transferred' surface to that of a 'fresh surface' prepared by etching in situ using a Xe ion PFIB.

To carry out manual CSEHI additional information is required. We use DOS models for likely compounds retrieved from the Materials Project open database using the Pymatgen application programming

interface [54] to define energy ranges for the manual CSEHI. Relevant DOS models were returned from a search of the Materials Project database for compounds of Li plus any of H; C; N; O. These compounds include products formed on the highly reactive LMA surface by a deliberate and limited exposure to air, moisture, and N_2 (described in SI section 2.1.1) [47,48].

4.1.2. Results and discussion

The SE spectra shown in Fig. 2 "Lithium metal" column is derived from 'platelet' (red) and 'surround' (blue) morphologies (determination of morphologies is described in Fig. S1). The energy ranges used for manual CSEHI were defined as red (0–3.5 eV) and blue (3.5–7.0 eV). These ranges were chosen based on DOS models. Red colouring of the energy region (0–3.5 eV) corresponds to possible LiH; Li_2N; Li; $LiHO_2$; Li_3N; Li_2O and LiH_3O_2 surface chemistries, while blue colouring in the 3.5–7.0 eV range corresponds to possible Li_2O_2, $Li(CO)_2$, Li_2CN_2, LiH_2CO_3, LiH_3O_2, Li_2CO_3 and LiHO Gaussian mixture models (GMMs) of DOS models overlaid with energy ranges are shown in Fig. 3). Chemical compound notation is in the form returned from the Materials Project database.

A CSEHI map obtained from Li surfaces using the colour assignment based on the DOS models shown in Fig. 3 is consistent with previous reports that a combination of passivation layer (formed during manufacture) and corrosion layer formed during glovebox storage and transfer exist on the commercial LMA surface [47]. However, due to the spatial averaging of previous surface chemical analysis approaches, the spatial distribution of these layers is unknown. The CSEHI image (Fig. 2, "Lithium metal" column) produced using input from DOS models provides the first visualisation of sub-micrometre scale Li metal surface chemical heterogeneity map as showing the contrast between red 'platelets' (average width 255 (120) nm) and blue 'surround' regions.

In order to confirm whether this sub-micrometre scale inhomogeneity of chemistry and 'platelet' morphology is typical of the LMA surface, four more regions were coloured with the energy ranges R (0–3.5 eV) and B (3.5–7.0 eV) (Figs. S3a and 3b). SE spectra plotted from red and blue regions of interest (ROIs) (Figs. S3c–f) were distinct. In the energy range 2.6–3.2 eV where red coloured areas had higher intensity whereas in the 3.4–4.2 eV energy range blue coloured areas had higher intensity. This shows that SEHI with CSEHI segmentation can differentiate the LMA surface chemistry based on characteristic SE spectra (Fig. S3h). While the 'platelet' morphology was not observed in these regions, the inhomogeneous surface chemistry as indicated by the presence of sub-micrometre red and blue regions was confirmed in all areas.

For a further check of the validity of our colour assignment and chemical speciation by DOS models, we exploit the phenomenon of electron beam induced deposition (EBID) of adventitious hydrocarbons that is well known to occur during prolonged electron beam exposure. This is done by imaging the previously imaged 10 μm horizontal field width (HFW) acquisition areas again at lower magnification (20 μm HFW) to check if the adding of material due to EBID to the original LMA surface could be observed (Fig. S4). The central 10 μm HFW EBID region was observed to have more blue colouring and darker edges than the saturation threshold set for segmentation. This result supports the rationale of relating colours to chemical species by DOS models, since the blue range is expected to indicate Li + C compounds (Fig. 3b) and EBID in the LV-SEM has been shown to deposit carbonaceous SEM chamber contamination [8]. The SE spectra post 10 μm HFW acquisition show a larger variation within regions that reduces the distinctness of regions of ROI spectra Fig. S4. This indicates that the EBID contains different species to those present on LMA as-transferred to the SEM.

However, the production of a Li metal surface chemistry by PFIB etch as opposed to other compounds ranked highly in the red range (0–3.5 eV) (eg. Li_2O; Li_3N; Li_2N), was not determined by the manual CSEHI method. To differentiate between compounds grouped in the red range (0–3.5 eV), a more detailed peak analysis would have to be made. SE spectroscopy may be well placed to deliver this, as the low energy SE peaks are strongly affected by chemical shift; with neighbouring atoms influencing the atomic energy levels determined by the distance from the nucleus. This effect can be observed by comparing DOS models for Li_2O and Li_2O_2. These compounds are not easily differentiated by XPS' exploitation of core level photoelectron emissions, as core energy levels are less affected by chemical shift [47].

To investigate the properties of any passivating layer on the as-transferred LMA surface, a fresh area of LMA surface was produced by controlled etching using the Xe ion beam of the PFIB over 10 × 10 μm

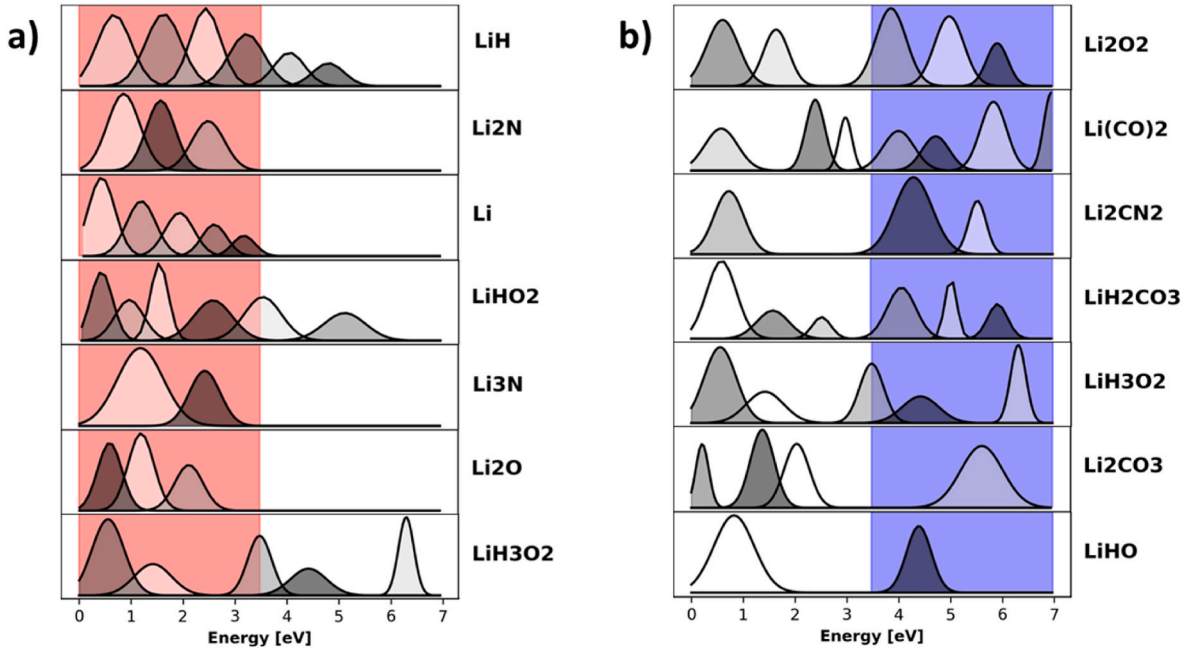

Fig. 3. The red (0–3.5 eV) and blue (3.5–7.0 eV) energy ranges overlaid on GMMs of DOS models to show the proportion of DOS within each energy range. The compounds are ranked by the area under the GMM curves within the energy range. The top 7 compounds (out of a total of 16) are displayed. The fitting of GMMs to the DOS models is described in Fig. S2.

areas (Figs. S5a and S5b). This etched area served as a reference versus the surrounding as-transferred LMA surface. Repeated measurements over four etched areas show that SE spectra from the etched and as-transferred regions (Fig. 4a) were consistently distinct, and that the etched region has higher emission intensity throughout the R (0–3.5 eV) energy range where the lithium metal signal is expected to be greatest according to reference DOS models.

Meanwhile, colour thresholding a CSEHI map produced from one of these etch regions (Fig. 4b) shows that the red colour associated with Li metal (as well as other compounds ranked in Fig. 3a) is localised to the region of etching. The distribution of blue to the left and top of the etch region, indicates the presence of lithium and carbon based compounds in a transition region of incomplete dose delivery caused by the ion beam tails. For data acquisition, the image contrast is adjusted so as not to saturate to the brightest region of the image (the etch square), and thus the as-transferred surface is included in the dark region of the segmented image (Fig. 4c). The proportion of emissions in the 0–3.5 eV versus the 3.5–7.0 eV ranges can be used as the as-transferred baseline. In the etch region the proportion of 0–3.5 eV emissions is increased compared to the 3.5–7.0 eV emissions, indicating a removal of Li + C compounds by the Xe ion etching.

4.1.3. Significance and impact

The manual CSEHI maps of LMA surface chemistry demonstrate the ability of this technique to detect and map surface inhomogeneity in lithium compounds at the sub-micrometre scale. Image resolution is 13.0 nm (measured by edge response [55]). This capability is complimentary to EDX analysis, where it is difficult to differentiate such compounds [18], and also to chemically sensitive but spatially averaging methods such as XPS [47]. Visualising heterogeneity at this scale is valuable to the understanding and development of a series of lithium-based batteries, such as the lithium-ion battery, lithium-air battery, lithium-sulphur battery, and all-solid-state lithium metal battery. The development of a standard database containing SE spectra of relevant compounds could be envisaged in the future. At present, it is difficult to identify the compounds of lithium within the colour regions of the manual CSEHI image. One means of overcoming this would be to identify colour energy ranges more specific to peaks in the reference DOS models. The possibility of using an automated CSEHI approach to determine colour energy ranges is demonstrated in section 5.

4.2. Peacock feather: knowledge from zoology

4.2.1. Background

For the majority of natural materials, DOS models such as those employed in section 4.1.1 are not available. However, the mapping of chemical variations on the sub-micrometre scale is the key towards understanding the structure, mechanism and process by which complex hierarchical self assembly occurs in Nature. This is of great scientific and commercial interest as it can often lead to future sources of bio-inspiration, for example the mechanical prowess of spider silk [56] and colouration seen in feathers. However, beam sensitivity coupled with a low signal yield at high electron beam voltages makes analysis by most electron microscopy analysis techniques extremely challenging for these materials.

In an entirely novel application of SEHI and CSEHI, spectra of a section of an iridescent male peacock (*Pavo cristatus*) feather were collected, as shown in Fig. 2, "Peacock feather" column. In the iridescent feather, barbules of a peacock the melanin-rich pigment cells (melanosomes) lie on the outside of the structure, whilst the overall structure is primarily composed of the proteinaceous structural polymer keratin [57].

Could CSEHI maps detect chemical differences between the melanin-rich edge of the feather barbule and the keratin-rich centre?

4.2.2. Results and discussion

Through the SE spectrum, we are able to assign energy levels where keratin (0–1.85 eV) and melanin emissions are more prominent (>1.85 eV). We assign the colours red and blue to these energy ranges respectively, to yield an image in which the blue colour should indicate the location of the melanosomes while other structures remain red. Note that the colours have been chosen here to provide a suitable contrast to those with impaired colour vision. The resulting CSEHI map allows the distinction between organic components, such as melanin and keratin, without the use of stains is evident. It is hypothesised that differences in the SE spectra for keratin and melanin may be a response to each polymer's unique chemical bonding as SEHI has already demonstrated the ability to map functional groups distribution in a range of polymer systems [7].

4.2.3. Significance and impact

In this instance, it is considered that the differences in the spectra around the peak at 1.1 eV observed in the keratin is attributable to disulphide bridges. If so, further validation of the results may provide new avenues for research based on this technique for protein analysis. For example, using CSEHI for the analysis of hair in the field of commercial cosmetics has the potential to provide new insights into product development [58].

4.3. Spider silk: using published SEHI energy range information

In looking towards material applications for these methods, we illustrate the benefit of using CSEHI for analysis of a spider dragline silk fibre (Fig. 2, "Spider silk" column). As hypothesised in relation to the peacock feather, if the SE emission peak observed at 1.1 eV is attributable to disulphide bridges it should be present in spider silk, as disulphide bridges have been proposed to explain spidroin dimerization in some species [59–61] and may be involved in fibre formation and improved mechanical properties [62,63]. This energy range is represented in red and is notably present within the ordered nanostructures (green) (average width 45 (10) nm) while the lower order bulk (4–6eV) remains blue [64]. Image resolution is 10.5 nm (measured by edge response [55]). Thus, CSEHI maps of silks should be informative for studies focused on fibre formation processes or modelling of mechanical

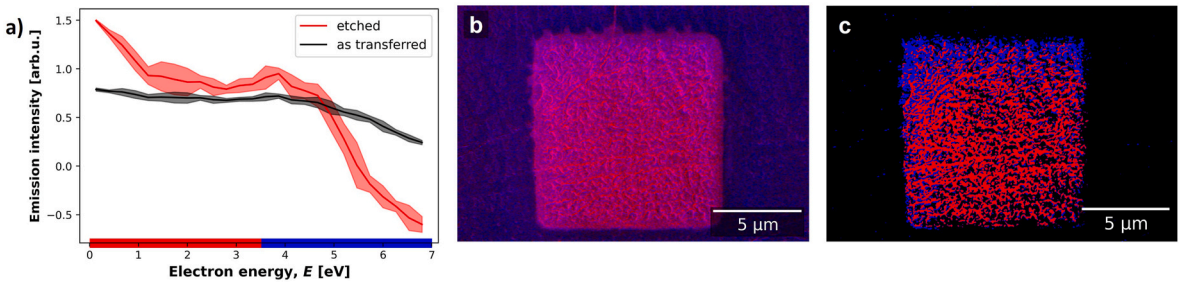

Fig. 4. (a) SE spectra from the etched and as-transferred regions. (b) CSEHI map of red (0–3.5 eV) and blue (3.5–7.0 eV) energy ranges, etched region (central 10 × 10 µm square) and as-transferred surface (darker surround region). (c) Image segmented by HSV (hue, saturation, value) colour space thresholding.

behaviour as the distribution of the nanostructures influences the mechanical properties of silk [65].

4.4. Historical pigments: knowledge of pigment compounds

4.4.1. Background

The painting sample originates from wall murals in the church of St. Gallus in Kuřívody, Northern Bohemia. Knowledge about the precise composition of the paint pigments can inform decisions about the correct techniques to employ in the restoration of valuable historic paintings as well as in art authentication [34]. Mineral pigment phases which are present in paintings in low quantities may be of major significance but are known to degrade over time and are only partially preserved [44].

Historical pigment samples are commonly analysed using Raman spectroscopy X-ray fluorescence (XRF) analysis and SEM-EDX analysis. These methods frequently reach their capability limits in terms of spatial resolution and information content. Some mineral phases are insufficiently Raman active and may not be detectable by the technique where they exist in only small quantities. Fluorescent X-ray energies may be too close to discern between elements by XRF or SEM-EDX. For example, the As 10.543 keV KL_3 emission and Pb 10.552 keV L_3M_5 emission [66]. By sensitivity to chemical bonding, CSEHI may allow identification of pigments containing such elements.

To demonstrate CSEHI in applications regarding optical properties of inorganic pigments, we consider the ability of SEHI to differentiate minerals cerussite ($PbCO_3$) and orpiment (As_2S_3) which are relevant to cultural heritage research due to their use as pigments in medieval times [44].

4.4.2. Results and discussion

The colouring ranges, 1.0–1.7 eV (red) and 3.0–3.7 eV (blue), were chosen with reference to DOS models of cerussite ($PbCO_3$) and orpiment (As_2S_3) (Figs. S8a and b) as compounds likely to be found in the historic painting sample (Fig. 1, "Historical pigments" column). Red colouring is expected to indicate a higher proportion of $PbCO_3$ while blue indicates As_2S_3 due to the absence of densities of states in 3–4 eV range in the $PbCO_3$ DOS model. The presence of DOS information in the experimental SE spectra from these materials was tested by preparing a reference material of the two pigments (SI section 2.4.1). The SE spectra from the two pigments is distinct in the 3–4 eV range where As_2S_3 has higher emission than the SE spectra from $PbCO_3$ (Fig. S8c).

4.4.3. Significance and impact

Here we show that CSEHI has the capability of mapping different sub-microscale (image resolution found to be 16.4 nm by edge response measurement [55]) mineral phases quickly and based on material properties beyond elemental composition and Raman selection rules.

5. Evaluation of CI framework using automated CSEHI

Automated CSEHI is developed to quickly evaluate the presence of spectral differences in the SE signal that result from materials surface chemistry. The automated CSEHI returns energy ranges to input to CSEHI. Up to now, the application of CSEHI has required either some background knowledge about the material system under investigation or the availability of SE spectra from relevant reference materials. An outstanding question remains: can CSEHI deliver informative maps without such additional, and likely user biased, inputs using an automated approach? In the following sections, we apply both the manual and automated framework for CSEHI to various materials and evaluate the information in automated CSEHI generated images.

5.1. Lithium metal surfaces

5.1.1. Results and discussion

In the case of the LMA (Fig. 5, "Lithium metal" column) the automated CSEHI framework seeks to identify three energy ranges corresponding to the available RGB image colour channels. However, by repeating the NNMF component analysis up to 16 times and selecting the most frequent output ranges, only two energy ranges were identified by the algorithm, at 0.1–1.1 eV and 1.1–1.8 eV.

In order to interpret the colour ranges returned by the automated application of CSEHI, ranges were overlaid on GMMs of DOS models of compounds (Fig. 6). A measure of the likelihood of a compound being coloured red or blue was determined by ranking the compounds by the area under the GMM curve in the red or blue ranges. The highest seven compounds in the red range were found to be LiH_3O_2, Li_2O, LiHO, Li, Li_2O_2, LiH_2CO_3 and $LiHO_2$. The highest seven compounds in the blue range were found to be Li_2N, Li_2CO_3, Li_3N, LiCN, $LiHO_2$, Li and LiH. By ranking the compounds this way, we expect lithium oxides and lithium hydroxides to be coloured red and lithium nitrides and lithium carbonates to be coloured blue.

The 1.1–1.8 eV range identified by automated CSEHI appears to be to be sensitive to lithium nitride compounds (Fig. 6b). By identifying colour ranges below 3.5 eV it may be possible to differentiate between oxides and nitrides, whereas in manual colouring all emissions below 3.5 eV were assigned to the red channel. The red 'platelet' morphology observed in the manual CSEHI image (Fig. 5 "Lithium metal" column) is still visible in the automated CSEHI image while the surrounding regions are darker. To interpret the image returned by automated CSEHI, the image was segmented by colour and brightness thresholds (Fig. S13). It is evident that the platelet regions are a mix of red and blue, in contrast to the darker surrounding regions. Therefore, in the platelet region it is probable that surface chemistry is a mixture of oxides, hydroxides and nitrides of lithium with heterogeneous distribution at the nanoscale. In the dark region, it is possible that compounds with low emission intensity are below the brightness threshold selected for segmentation. The compounds expected to have a low emission intensity in the red and blue ranges are $Li(CO)_2$, Li_2CN_2, LiH and $LiHO_2$.

The automated workflow was also applied to produce a CSEHI map of the PFIB etched LMA surface (Fig. 7a). The threshold segmented image (Fig. 7b) shows that the red and blue ranges predominantly coloured the etched region while the surrounding as-transferred surface is below the colour saturation threshold. As with the energy ranges returned by the automated workflow applied to the as-transferred LMA surface, the energy ranges are narrower and provide more specificity to the identification of lithium compounds. The energy ranges returned predict a higher extent of Li_2O, Li_2N and Li in the red region (Fig. 7d) while Li_2O_2, Li_2CN_2 and LiH_3O_2 compounds fall within the blue region (Fig. 7e). Comparison of the as-transferred (dark) and etched (red and blue) low energy ranges shows higher emission in the low energy region indicative of lower oxidation state lithium compounds (Fig. 7c).

The result of a heterogeneous surface lithium oxide and lithium nitride distribution at the nanoscale on the as-transferred LMA surface does not match the model of a LMA surface made up of uniform and depth stratified layers of Li_2CO_3, LiOH and Li_2O [47,67]. It is more similar to a surface with 'local inorganic and organic contaminants' produced by storage and transfer from an Ar filled glovebox and described by Otto et al. The influence of surface chemical attack by contaminants has also been observed in the electrochemical performance of a lithium metal electrode [48]. Thus, SEHI could be used to develop models of the lithium metal surface post passivation and corrosion, especially in terms of the spatial distribution of surface chemistry.

5.1.2. Significance and impact

Here we have shown that SEHI may be well placed to differentiate the lithium-carbon compounds, lithium hydroxide and lithium nitride

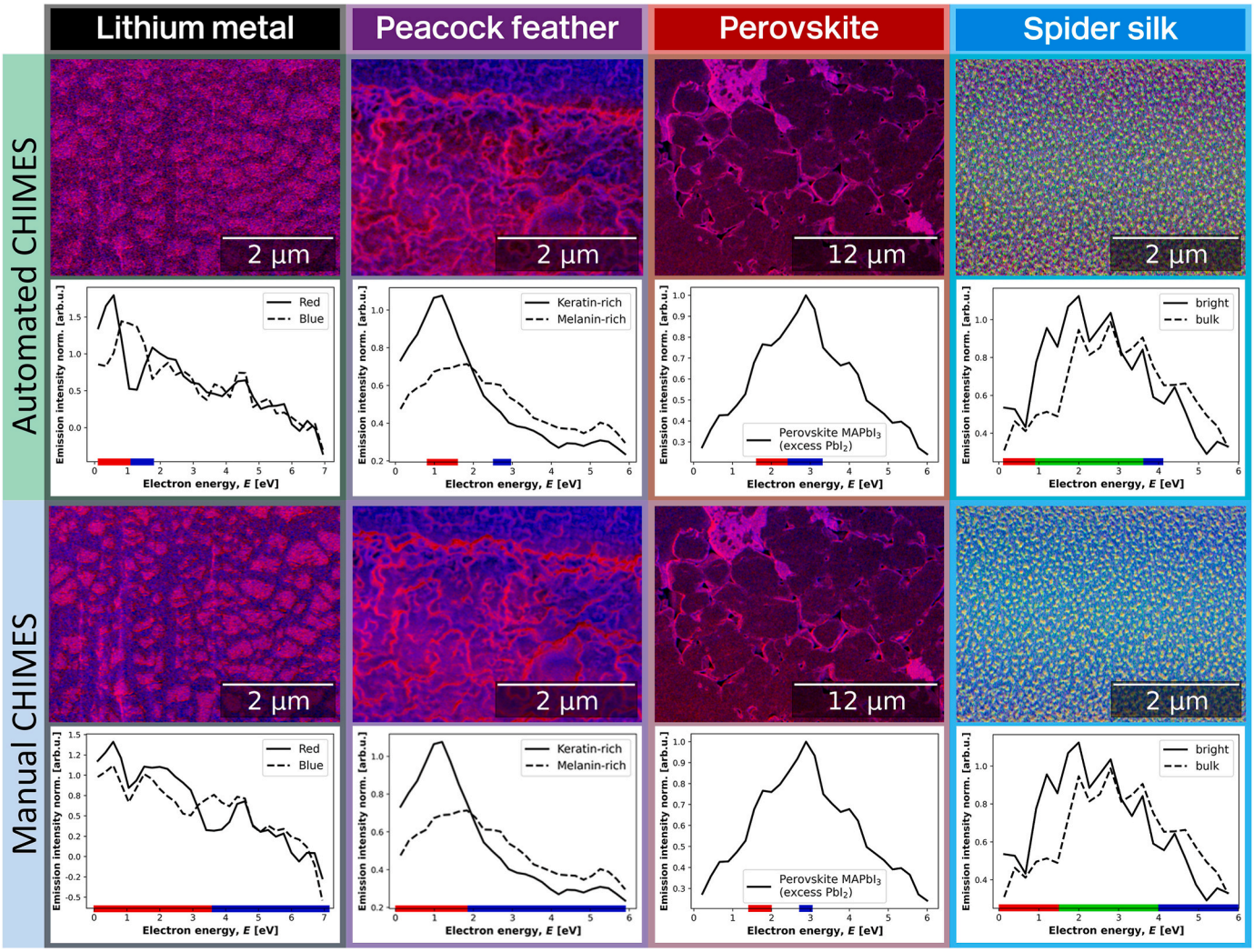

Fig. 5. Comparison of automated and manual CSEHI results, with their respective spectral colour ranges.

surface chemistries. The characterisation and identification of these lithium compounds is important, as these compounds are critical areas of study for LMBs and other lithium-based batteries. For example, Li_2CO_3, Li_2O, Li_3N, LiOH, LiH (and $LiOH{\cdot}H_2O$) are major components of a SEI layer in the lithium metal [68–70] and lithium-sulphur battery [71]. Effects of Li_2O and Li_2O_2 formed at a cathode/solid-state-electrolyte ($LiCoO_2$/lithium phosphorus oxynitride) interface could cause high impedance and subsequent capacity decay [72]. The water content in an electrolyte solution can also affect interface reaction mechanisms, which could be confirmed by the formation of $LiHO_2$ [73,74]. Yet there are still uncertainties on the parasitic reactions occurring at the electrolyte-LMA interfaces [75]. The chemical information derived here may be used to answer to key lithium-related electrochemical questions, either by characterising adventitious surface chemistries, or those that form via electrochemical reactions.

Spatially resolved surface chemical analysis can also shed new light on the sub-micrometre heterogeneity of the LMA where spatially averaging surface analysis techniques cannot. SEHI's application within a (P) FIB-SEM also demonstrates the further capability of depth resolved chemical analysis to investigate existing models of the LMA passivation layers [47,67].

Comparison of the as-transferred and etched LMA surfaces showed that SEHI may differentiate the two conditions by characteristic SE spectra. Furthermore, energy ranges returned by automated CSEHI assist in identification of surface chemistry by comparison to DOS models. The ranking of compounds by area within the energy range shows that the oxidation state of the lithium surface compounds is reduced by plasma etching. Future SEHI experiments should look to verify the identification of chemical species made here (by reference to DOS) by using reference samples and correlative analysis with chemical and surface sensitive analyses such as XPS and TOF-SIMS.

5.2. Peacock feather

5.2.1. Results and discussion

Fig. 8 displays both the manual and automated coloured peacock feather CSEHI images (Fig. 8a), each with a ROI taken from the same region (Fig. 8b). This allows for a direct comparison of the colouring of manual and automated CSEHI images with a model of the structure of a peacock feather previously proposed (Fig. 8c). The model predicts: keratin (dots) and tonofibrillen (dashed lines) both of which contain disulphide bonding, melanin (black structures) and air pockets (white regions). All model predictions are present and are shown within both SEHI images, however, it is observed that the automated image has greater localised specific intensity. This is especially prominent in identifying air pockets as reductions in colour intensity resulting in a visible 'blur' of colour within the manual image and absence of colour within the automated image. The reason for these observed differences is that the automated process provides smaller energy ranges. SE emissions outside the energy range do not contribute to pixel intensity, and

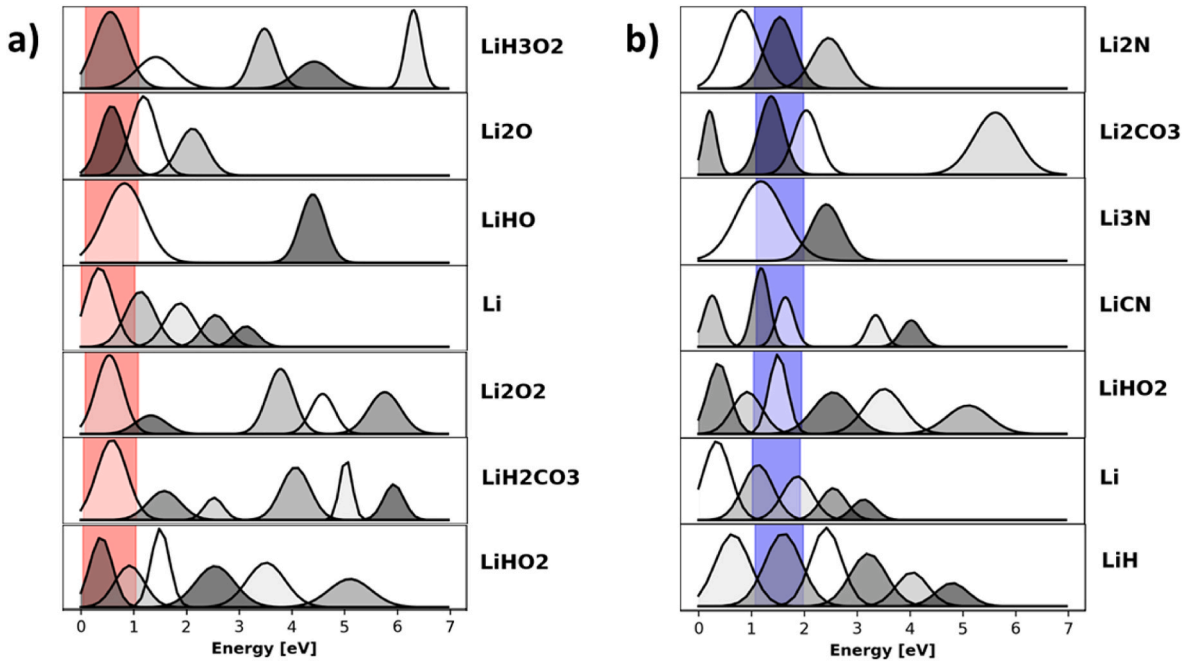

Fig. 6. (a) red (0.1–1.1 eV) and (b) blue (1.1–1.8) colour ranges overlaid onto GMMs of Li compound DOS models. The compounds are ranked by the area under the curve in each colour range. For example, the compound with the largest area under the curve in the red range was LiH_3O_2.

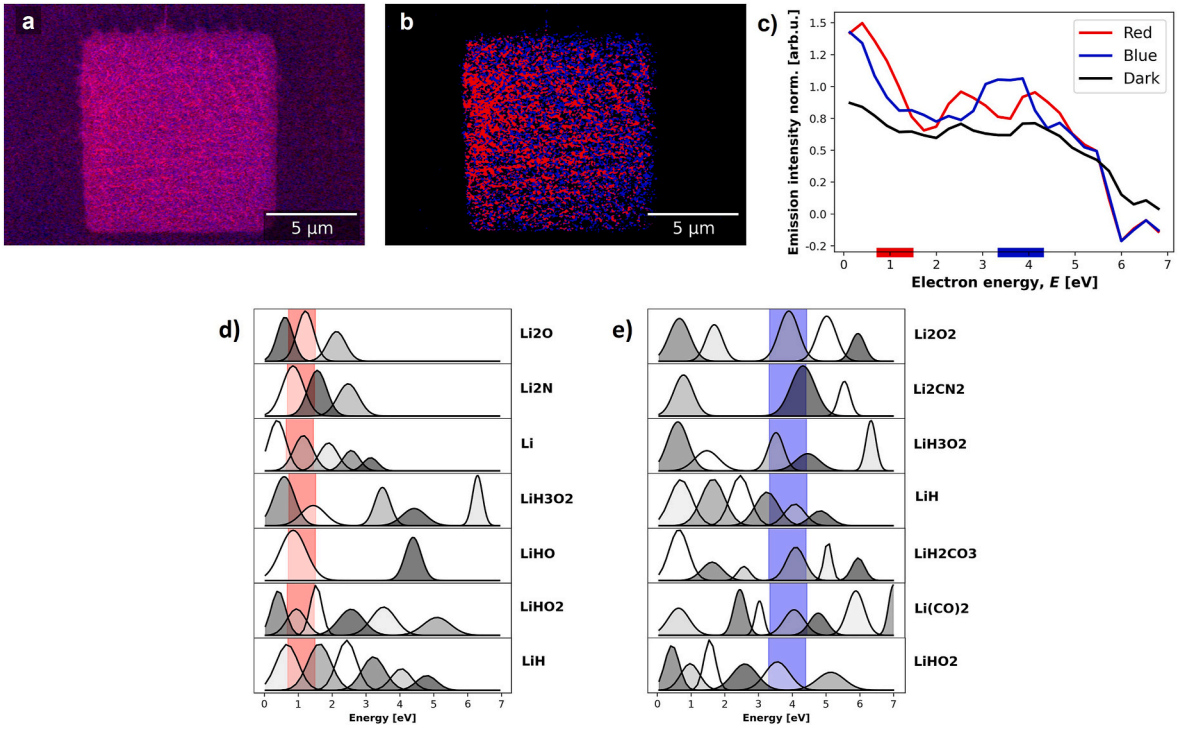

Fig. 7. (a) Automated CSEHI map of the etched LMA surface. (b) HSV colour space threshold segmented image from which (c) spectra are plotted. (d and e) Automated CSEHI red (0.7–1.5 eV) and blue (3.3–4.4 eV) energy ranges overlaid on GMMs of DOS models of likely Li compounds.

this results in the automated image having higher contrast, as seen in line profiles from CSEHI images (Fig. 8d). An automated approach therefore allows for a more precise colour representation of the known model both for reducing 'blurring' effects and also to emphasise more pronounced structures, such as those of the di-sulphide bonding.

5.2.2. Significance and impact

Despite both the manual and automated SEHI images showing di-sulphide bonds (coloured red) correctly in both keratin and tonofibrillen regions, the automated colouring process provides far greater specific colour sensitivity allowing for greater insights into localised structures. Being able to identify localised di-sulphide bonding is of great interest in many research fields from the obvious use in the development of cosmetics to other diverse fields such as archaeology. Studies have shown that through characterising the shape and size of melanosomes, researchers are confident that they can unlock the colour

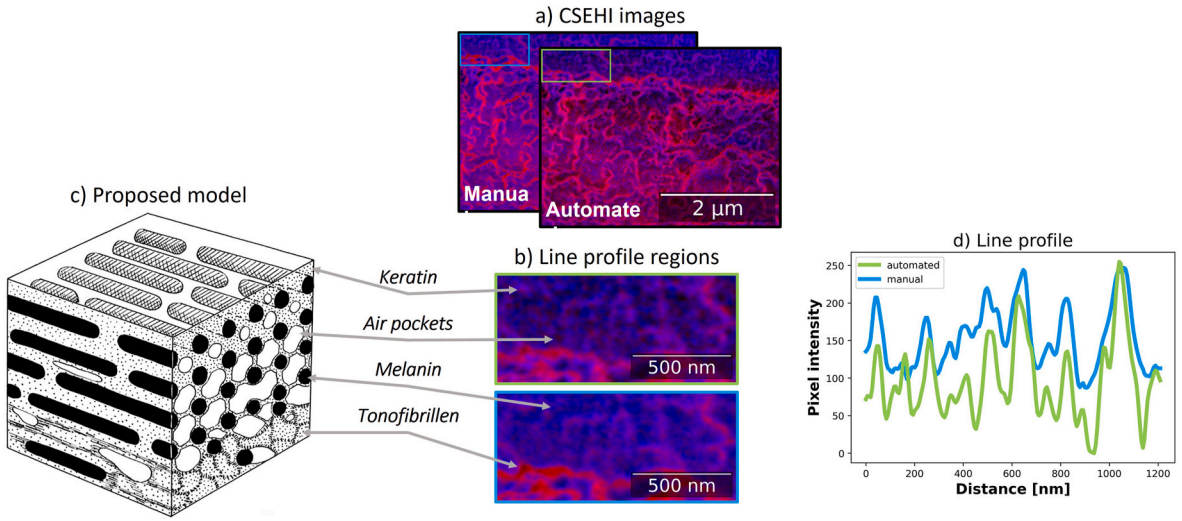

Fig. 8. (a) Automated and Manual SEHI stacks collected from a Peacock Feather. (b) Two regions of interest of SEHI images presented in (a). (c) presents a model of the structures of a Peacock feather as adapted from Ref. [76] under creative commons license CC BY-NC-SA 3.0, https://creativecommons.org/licenses/by-nc-sa/3.0/. (d) Presents the line intensity profiles of both regions shown in (b).

of non-iridescent structural feathers using fossil records. A SEHI approach has the potential to provide further analysis capabilities for the identification and characterisation of melanosomes using specific di-sulphide bonding distributions enabling them to act as a fingerprint to reveal from the fossil record an accurate colour identification of feathers [76].

5.3. Perovskite solar cell material

5.3.1. Background

A system where the presence of phase separation affects functionality and lifetime are organic–inorganic hybrid lead halide perovskites used for high efficiency solar cells [77]. The solar cell material studied here is methylammonium lead iodide ($MAIPbI_3$) with 5 mol% excess methyl ammonium iodide (MAI).

5.3.2. Results and discussion

Tracking excess PbI_2 within hybrid lead halide perovskites is possible (Fig. 5, "Perovskite"). Using the automated colouring, without any additional information from reference materials, results in a similar image to that produced by manual colouring based on the energy ranges previously identified [78]. Kumar et al. show that energy range between 1.4 and 2.0 eV represents either MAI or $MAPbI_3$ perovskite. The automated approach has picked up a range between 1.6 and 2.4 eV. Although this covers a wider energy range than in the manually coloured image, both images highlight the same areas where in addition to the perovskite, excess PbI_2 is present. Note the energy range for excess PbI_2 was manually identified in Ref. [78] to be in the range of 2.7–3.3 eV. The automated approach finds a corresponding energy range covering an energy range from 2.4 to 3.3 eV but does not identify a third reliable energy range.

5.3.3. Significance and impact

The automated CSEHI result identified phase separation in the solar cell material into two phases by identifying an energy range associated with $MAI/MAIPbI_3$ (red) and PbI_2 (blue). The presence of two phases is verified by previous experimental work using reference materials [78]. The spatial distribution of these phases is visualised in the automated CSEHI image, with no additional input information.

5.4. Spider silk

Previously published SE data for spider silk did not make use of NNMF [64]. Instead, a manual identification process was used to separate energy ranges with high SE emission from ordered nanostructures and disordered matrix, respectively, on silk fibres. The outermost layer of which comprises a 'coating' consisting of lipids and glycoproteins [64]. The red regions in the automated CSEHI image indicates the location of remnants of the coating. The green in the automated CSEHI falls well within the energy range that was previously manually identified to be associated with ordered nanostructures. Thus, the automated CSEHI image reflects the structure of the fibre. Similarly, blue represents the disorder matrix in the automated CSEHI image, again in agreement with prior manual allocation [64].

6. Summary and conclusion

The CSEHI method enables the visualisation of inhomogeneity of chemical phases at a glance. In the example materials from energy harvesting and storage, art history and zoology, CSEHI maps revealed varying surface chemistry on bulk functional materials down to the nanoscale. For instance, automated CSEHI differentiated lithium-carbon compounds, lithium hydroxide and lithium nitride surface chemistries on a LMA and highlighted di-sulphide bridge related nanostructures in peacock feather and spider dragline silk.

Automated and manual CSEHI results were evaluated by comparison to DOS models, controlled changes to surface chemistry, reference materials and previously published energy ranges. In the LMA example, the CSEHI method combined with DOS model comparison was used to trace and rank likely surface lithium species. The manual CSEHI method can reveal the presence of surface chemical variations but is less suited to the identification of chemical phases due to wide energy windows given the limited additional information in the absence of a reliable SE spectroscopy reference repository or dedicated SE spectrum models for complex functional materials. Thus, phases with an SE spectrum peak in a similar energy range can be conflated into the same colour. Future work should consider using alternative colour spaces to RGB to allow mapping of more than three energy ranges and therefore map chemical phases with more specificity.

The automated CSEHI method tends to deliver colour ranges over narrower energies and is more suited to phase identification. Thus, automated CSEHI has the potential to reduce nanoscale CI bottlenecks

by making SEHI and visualisation of surface chemical distribution down to the nanoscale accessible to a broad user base. Additionally, the method can be applied in data-driven materials science since the user does not expect to have background knowledge of the samples.

Credit author statement

James F. Nohl: Methodology, Software, Validation, Formal analysis, Investigation, Data curation, Writing – original draft, Writing – review and editing, Visualisation. Nicholas T. H. Farr: Methodology, Visualisation, Validation, Formal analysis, Investigation, Resources, Data curation, Writing – original draft, Writing – review and editing. Yige Sun: Methodology, Investigation, Resources, Data curation, Writing – review and editing. Gareth M. Hughes: Methodology, Investigation, Resources, Data curation, Writing – review and editing. Nicola Stehling: Methodology, Software, Validation, Formal analysis, Investigation, Resources, Data curation. Jingqiong Zhang: Software, Formal analysis, Data curation, Writing – original draft. Fodio Longman: Software, Formal analysis, Data curation. Gemma Ives: Software, Validation, Data curation. Zuzana Pokorná;: Writing – review and editing. Filip Mika: Investigation, Resources, Writing – review and editing. Vikas Kumar: Investigation, Resources, Data curation. Lyudmila Mihaylova: Validation, Writing – review and editing. Chris Holland: Resources, Writing – review and editing, Supervision, Project administration. Serena A. Cussen: Writing – review and editing, Supervision, Project administration, Funding acquisition. Cornelia Rodenburg: Conceptualisation, Methodology, Writing – original draft, Writing – review and editing, Supervision, Project administration, Funding acquisition.

Declaration of competing interest

The authors declare that they have no known competing financial interests or personal relationships that could have appeared to influence the work reported in this paper.

Data availability

The data, processing code and packaged MATLAB application are available to download.

Data for 'Insights into surface chemistry down to nanoscale: An accessible colour hyperspectral imaging approach for scanning electron microscopy' (Original data) (Figshare) (https://doi.org/10.15131/shef.data.14780082)

CSEHI MATLAB application (Data processing application) (https://doi.org/10.15131/shef.data.21647090)

pysehi releases (Data processing code) (Figshare) (https://doi.org/10.15131/shef.data.22310068)

Acknowledgements

C.R. thanks the EPSRC for funding under SEE MORE: Secondary Electron Emission-Microscopy for Organics with Reliable Engineering Properties (EP/N008065/1). C.R., L.S.M. and J.Z. thank the EPSRC for funding under SEE MORE MAKE MORE (EP/V012126/1), N.T.H.F. for fellowship (EP/T517835/1) and J.F.N. for support from the Faraday Institution through project FutureCat (FIRG017). Y.S. thanks the Faraday Institution for financial support through project Nextrode (FIRG015) and the support from the David Cockayne Fellowship at Linacre College, University of Oxford. S.C. acknowledges support from the Engineering and Physical Sciences Research Council (EP/N001982/2) and the Faraday Institution (grant numbers FIRG017 and FIRG001). C.H. was supported by EPSRC Fellowship EP/K005693/1. Z.P. and F.M. acknowledge support from The Czech Academy of Sciences (project RVO:68081731 and Strategy AV21, Breakthrough future technologies). Electron microscopy and analysis was performed in the Sorby Centre for Electron Microscopy at the University of Sheffield. G.M.H. and Y.S acknowledge the use of characterisation facilities within the David Cockayne Centre for Electron Microscopy (DCCEM), Department of Materials, University of Oxford, alongside financial support provided by the Henry Royce Institute (Grant ref EP/R010145/1).

Appendix A. Supplementary data

Supplementary data to this article can be found online at https://doi.org/10.1016/j.mtadv.2023.100413.

References

[1] W. Han, M. Zheng, A. Banerjee, Y.Z. Luo, L. Shen, A. Khursheed, Quantitative material analysis using secondary electron energy spectromicroscopy, Sci. Rep. 10 (1) (Dec 2020).
[2] A. Khursheed, Secondary Electron Energy Spectroscopy in the Scanning Electron Microscope, World Scientific, Aug 2020.
[3] N.T.H. Farr, S.F. Hamad, E. Gray, C.M. Magazzeni, F. Longman, D.E.J. Armstrong, J.P. Foreman, F. Claeyssens, N.H. Green, C. Rodenburg, Identifying and mapping chemical bonding within phenolic resin using secondary electron hyperspectral imaging, Polym. Chem. 12 (2) (2021) 177–182.
[4] R.C. Masters, A.J. Pearson, T.S. Glen, F.-C. Sasam, L. Li, M. Dapor, A.M. Donald, D. G. Lidzey, C. Rodenburg, Sub-nanometre resolution imaging of polymerfullerene photovoltaic blends using energy-filtered scanning electron microscopy, Nat. Commun. 6 (1) (Apr 2015).
[5] Q. Wan, K.J. Abrams, R.C. Masters, A.C.S. Talari, I.U. Rehman, F. Claeyssens, C. Holland, C. Rodenburg, Mapping nanostructural variations in silk by secondary electron hyperspectral imaging, Adv. Mater. 29 (47) (Nov 2017), 1703510.
[6] K.J. Abrams, Q. Wan, N.A. Stehling, C. Jiao, A.C.S. Talari, I. Rehman, C. Rodenburg, Nanoscale mapping of semi-crystalline polypropylene, Phys. Status Solidi C 14 (12) (Nov 2017), 1700153.
[7] N. Farr, J. Thanarak, J. Schäfer, A. Quade, F. Claeyssens, N. Green, C. Rodenburg, Understanding surface modifications induced via argon plasma treatment through secondary electron hyperspectral imaging, Adv. Sci. 8 (4) (Jan 2021), 2003762.
[8] N.T.H. Farr, G.M. Hughes, C. Rodenburg, Monitoring carbon in electron and ion beam deposition within FIB-SEM, Materials 14 (11) (Jun 2021) 3034.
[9] R. Rasch, A. Stricher, R.W. Truss, Energy filtered low voltage in lens detector SEM and XPS of natural fiber surfaces, J. Appl. Polym. Sci. 131 (9) (2013), 39572 (1-7).
[10] S. Asahina, M. Suga, H. Takahashi, H.Y. Jeong, C. Galeano, F. Schüth, O. Terasaki, Direct observation and analysis of yolk-shell materials using low-voltage high-resolution scanning electron microscopy: nanometal-particles encapsulated in metal-oxide, carbon, and polymer, Apl. Mater. 2 (11) (Nov 2014), 113317 (1-7).
[11] D. Mandal, M. Jadeja, N. Ghuge, D. Sen, S. Mazumder, Effect of excess lithium on sintering behaviour of lithium-titanate pebbles: modifications of microstructure and pore morphology, Fusion Eng. Des. 112 (Nov 2016) 520–526.
[12] D.C. Joy, Second best no more, Nat. Mater. 8 (10) (Oct 2009) 776–777.
[13] J.F. Nohl, Secondary electron hyperspectral imaging: nanostructure and chemical analysis for the LV-SEM, Mater. Sci. Technol. 36 (5) (Mar 2020) 527–539.
[14] A. Janssen, M. Burke, S. Burgess, "High spatial resolution spectrum imaging in the FEG-SEM at low voltages: a new option for materials characterisation,", in: European Microscopy Congress 2016: Proceedings, Wiley-VCH Verlag GmbH & Co. KGaA, Dec 2016, pp. 959–960.
[15] Various, "ColorSEM technology : faster information for faster discovery", Thermofisher Scientific, Tech. Rep. (2020).
[16] S. Burgess, J. Sagar, J. Holland, X. Li, F. Bauer, Ultra-low kV EDS - a new approach to improved spatial resolution, surface sensitivity, and light element compositional imaging and analysis in the SEM, Microscopy Today 25 (2) (Mar 2017) 20–29.
[17] A. Schoning, R. Lackner, A. Bechteler, A. Liebel, A. Niculae, H. Soltau, A compact high solid angle EDX detector system for SEM and TEM, Microsc. Microanal. 23 (S1) (Jul 2017) 76–77.
[18] P. Hovington, V. Timoshevskii, S. Burgess, H. Demers, P. Statham, R. Gauvin, K. Zaghib, Can we detect Li K X-ray in lithium compounds using energy dispersive spectroscopy? Scanning 38 (6) (Feb 2016) 571–578.
[19] C. Busà, M. Belekoukia, M.J. Loveridge, The effects of ambient storage conditions on the structural and electrochemical properties of NMC-811 cathodes for Li-ion batteries, Electrochim. Acta 366 (Jan 2021), 137358.
[20] G. Budnik, J.A. Scott, C. Jiao, M. Maazouz, G. Gledhill, L. Fu, H.H. Tan, M. Toth, Nanoscale 3D tomography by in-flight fluorescence spectroscopy of atoms sputtered by a focused ion beam, Nano Lett. 22 (20) (Oct 2022) 8287–8293.
[21] C. Cardell, I. Guerra, An overview of emerging hyphenated SEM-EDX and Raman spectroscopy systems: applications in life, environmental and materials sciences, TrAC, Trends Anal. Chem. 77 (Mar 2016) 156–166.
[22] Y.B. Zou, S.F. Mao, B. Da, Z.J. Ding, Surface sensitivity of secondary electrons emitted from amorphous solids: calculation of mean escape depth by a Monte Carlo method, J. Appl. Phys. 120 (23) (Dec 2016), 235102.
[23] N.B. Jackson, P.R. Chaurand, J.E. Fulghum, R. Hernandez, D.A. Higgins, R. Hwang, K. Kneipp, A.P. Koretsky, C.A. Larabell, S.J. Stranick, W.W. Webb, P.S. Weiss, N. Woodbury, X.S. Xie, E.S. Yeung. Visualizing Chemistry : the Progress and Promise of Advanced Chemical Imaging, National Academies Press, 2006.
[24] D. Lu, K. Goto, B. Da, J. Liu, H. Yoshikawa, S. Tanuma, Z. Ding, Secondary electron-, auger electron- and reflected electron-spectroscopy study on sp^2-

hybridization carbon materials: HOPG, carbon glass and carbon fiber, J. Electron. Spectrosc. Relat. Phenom. 250 (Jul 2021), 147086 (1-10).
[25] K.J. Abrams, M. Dapor, N. Stehling, M. Azzolini, S.J. Kyle, J. Schäfer, A. Quade, F. Mika, S. Kratky, Z. Pokorna, I. Konvalina, D. Mehta, K. Black, C. Rodenburg, Making sense of complex carbon and metal/carbon systems by secondary electron hyperspectral imaging, Adv. Sci. 6 (19) (Aug 2019), 1900719.
[26] J.F. Nohl, N.T. Farr, Y. Sun, G.M. Hughes, S.A. Cussen, C. Rodenburg, Low-voltage SEM of air-sensitive powders: from sample preparation to micro/nano analysis with secondary electron hyperspectral imaging, Micron 156 (May 2022), 103234.
[27] M. Burgstaller, Chemical colour imaging and its advantages by deploying hyperspectral cameras for industrial applications, NIR News 25 (6) (Sep 2014) 8–10.
[28] C. Kamath, Y.J. Fan, Data mining in materials science and engineering, in: Informatics for Materials Science and Engineering, Elsevier, 2013, pp. 17–36.
[29] H. Li, Z. Zhang, Z.-Z. Zhao, Data-mining for processes in chemistry, materials, and engineering, Processes 7 (3) (Mar 2019) 151.
[30] L. Himanen, A. Geurts, A.S. Foster, P. Rinke, Data-driven materials science: status, challenges, and perspectives, Adv. Sci. 6 (21) (Sep 2019), 1900808.
[31] S. Huang, J.M. Cole, A database of battery materials auto-generated using ChemDataExtractor, Sci. Data 7 (1) (Aug 2020).
[32] J.M. Cole, K.S. Low, H. Ozoe, P. Stathi, C. Kitamura, H. Kurata, P. Rudolf, T. Kawase, Data mining with molecular design rules identifies new class of dyes for dye-sensitised solar cells, Phys. Chem. Chem. Phys. 16 (48) (2014) 26684–26690.
[33] M. Krallinger, O. Rabal, A. Lourenço, J. Oyarzabal, A. Valencia, Information retrieval and text mining technologies for chemistry, Chem. Rev. 117 (12) (May 2017) 7673–7761.
[34] B.I. Łydzba-Kopcynska, J. Szwabinski, Attribution markers and data mining in art authentication, Molecules 27 (1) (Dec 2021) 70.
[35] M. Botifoll, I. Pinto-Huguet, J. Arbiol, Machine learning in electron microscopy for advanced nanocharacterization: current developments, available tools and future outlook, Nanoscale Horizons 7 (12) (2022) 1427–1477.
[36] D. Lee, H.S. Seung, Algorithms for non-negative matrix factorization, in: T. Leen, T. Dietterich, V. Tresp (Eds.), Advances in Neural Information Processing Systems, MIT Press, 2000, pp. 535–541.
[37] B. Bayar, N. Bouaynaya, R. Shterenberg, Pobabilistic non-negative matrix factorization: theory and application to microarray data analysis, J. Bioinf. Comput. Biol. 12 (1) (2014), 1450001.
[38] C.J. Long, D. Bunker, X. Li, V.L. Karen, I. Takeuchi, Rapid identification of structural phases in combinatorial thin-film libraries using x-ray diffraction and non-negative matrix factorization, Rev. Sci. Instrum. 80 (10) (Oct 2009), 103902.
[39] B. Ren, L. Pueyo, G.B. Zhu, J. Debes, G. Duchêne, Non-negative matrix factorization: robust extraction of extended structures, Astrophys. J. 852 (2) (Jan 2018) 104.
[40] I. Konvalina, F. Mika, S. Krátký, E.M. Mikmeková, I. Müllerová, In-lens band-pass filter for secondary electrons in ultrahigh resolution SEM, Materials 12 (14) (Jul 2019) 2307.
[41] N. Stehling, R. Masters, Y. Zhou, R. O'Connell, C. Holland, H. Zhang, C. Rodenburg, New perspectives on nano-engineering by secondary electron spectroscopy in the helium ion and scanning electron microscope, MRS Communications 8 (2) (Apr 2018) 226–240.
[42] P. Kazemian, S. Mentink, C. Rodenburg, C. Humphreys, Quantitative secondary electron energy filtering in a scanning electron microscope and its applications, Ultramicroscopy 107 (2–3) (Feb 2007) 140–150.
[43] S. Muto, M. Shiga, Application of machine learning techniques to electron microscopic/spectroscopic image data analysis, Microscopy 69 (2) (Nov 2019) 110–122.
[44] D. Hradil, J. Hradilová, P. Bezdička, S. Švarcová, Z. Čermáková, V. Košařová, I. Němec, Crocoite $PbCrO_4$ and mimetite $Pb_5(AsO_4)_3Cl$: rare minerals in highly degraded mediaeval murals in northern bohemia, J. Raman Spectrosc. 45 (9) (Jul 2014) 848–858.
[45] W. Xu, J. Wang, F. Ding, X. Chen, E. Nasybulin, Y. Zhang, J.-G. Zhang, Lithium metal anodes for rechargeable batteries, Energy Environ. Sci. 7 (2) (2014) 513–537.
[46] Y. Nishi, Lithium ion secondary batteries; past 10 years and the future, J. Power Sources 100 (1–2) (2001) 101–106.
[47] S.-K. Otto, Y. Moryson, T. Krauskopf, K. Peppler, J. Sann, J. Janek, A. Henss, In-depth characterization of lithium-metal surfaces with XPS and ToF-SIMS: toward better understanding of the passivation layer, Chem. Mater. 33 (3) (Jan 2021) 859–867.
[48] Y. Li, Y. Li, Y. Sun, B. Butz, K. Yan, A.L. Koh, J. Zhao, A. Pei, Y. Cui, Revealing nanoscale passivation and corrosion mechanisms of reactive battery materials in gas environments, Nano Lett. 17 (8) (Jul 2017) 5171–5178.
[49] B. Han, Z. Zhang, Y. Zou, K. Xu, G. Xu, H. Wang, H. Meng, Y. Deng, J. Li, M. Gu, Poor stability of Li_2CO_3 in the solid electrolyte interphase of a lithium-metal anode revealed by cryo-electron microscopy, Adv. Mater. 33 (22) (Apr 2021), 2100404.
[50] Y.-C. Hsieh, M. Leißing, S. Nowak, B.-J. Hwang, M. Winter, G. Brunklaus, Quantification of dead lithium via in situ nuclear magnetic resonance spectroscopy, Cell Reports Physical Science 1 (8) (Aug 2020), 100139.
[51] K.R. Adair, M.N. Banis, Y. Zhao, T. Bond, R. Li, X. Sun, Temperature-dependent chemical and physical microstructure of Li metal anodes revealed through synchrotron-based imaging techniques, Adv. Mater. 32 (32) (Jul 2020), 2002550.
[52] S. Oswald, Auger- and X-ray photoelectron spectroscopy at metallic Li material: chemical shifts related to sample preparation, gas atmosphere, and ion and electron beam effects, Batteries 8 (3) (Mar 2022) 24.
[53] J.E. Owejan, J.P. Owejan, S.C. DeCaluwe, J.A. Dura, Solid electrolyte interphase in Li-ion batteries: evolving structures measured in situ by neutron reflectometry, Chem. Mater. 24 (11) (May 2012) 2133–2140.
[54] S.P. Ong, W.D. Richards, A. Jain, G. Hautier, M. Kocher, S. Cholia, D. Gunter, V. L. Chevrier, K.A. Persson, G. Ceder, Python materials genomics (pymatgen): a robust, open-source python library for materials analysis, Comput. Mater. Sci. 68 (Feb 2013) 314–319.
[55] S.W. Smith, The Scientist and Engineer's Guide to Digital Signal Processing, California Technical Publishing, 1997, pp. 423–450, ch. 25: Special Imaging Techniques.
[56] Q. Wang, H.C. Schniepp, Strength of recluse spider's silk originates from nanofibrils, ACS Macro Lett. 7 (11) (Oct 2018) 1364–1370.
[57] J.M. Medina, J.A. Dáz, P. Vukusic, Classification of peacock feather reflectance using principal component analysis similarity factors from multispectral imaging data, Opt Express 23 (8) (Apr 2015), 10198.
[58] C.F. Cruz, M. Martins, J. Egipto, H. Osório, A. Ribeiro, A. Cavaco-Paulo, Changing the shape of hair with keratin peptides, RSC Adv. 7 (81) (2017) 51581–51592.
[59] A. Rising, H. Nimmervoll, S. Grip, A. Fernandez-Arias, E. Storckenfeldt, D. P. Knight, F. Vollrath, W. Engström, Spider silk proteins mechanical property and gene sequence, Zool. Sci. 22 (3) (Mar 2005) 273–281.
[60] T. Matsuhira, S. Osaki, Molecular weight of Nephila clavata spider silk, Polym. J. 47 (6) (Mar 2015) 456–459.
[61] A. Sponner, B. Schlott, F. Vollrath, E. Unger, F. Grosse, K. Weisshart, Characterization of the protein components of *Nephila clavipes* dragline silk, Biochemistry 44 (12) (Mar 2005) 4727–4736.
[62] S. Grip, J. Johansson, M. Hedhammar, Engineered disulfides improve mechanical properties of recombinant spider silk, Protein Sci. 18 (5) (May 2009) 1012–1022.
[63] S. Ittah, A. Michaeli, A. Goldblum, U. Gat, A model for the structure of the C-terminal domain of dragline spider silk and the role of its conserved cysteine, Biomacromolecules 8 (9) (Aug 2007) 2768–2773.
[64] N. Stehling, K.J. Abrams, C. Holland, C. Rodenburg, Revealing spider silks 3D nanostructure through low temperature plasma etching and advanced low-voltage SEM, Frontiers in Materials 5 (Jan 2019).
[65] F. Fraternali, N. Stehling, A. Amendola, B.A.T. Anrango, C. Holland, C. Rodenburg, Tensegrity modelling and the high toughness of spider dragline silk, Nanomaterials 10 (8) (Jul 2020) 1510.
[66] L. Hudson, "X-ray transition energies, NIST standard reference database 128," (2003).
[67] C. Naudin, J. Bruneel, M. Chami, B. Desbat, J. Grondin, J. Lassègues, L. Servant, Characterization of the lithium surface by infrared and Raman spectroscopies, J. Power Sources 124 (2) (2003) 518–525.
[68] S. Zhang, Y. Liu, H. Liu, Understanding lithium transport in SEI films: a nonequilibrium molecular dynamics simulation, Mol. Simulat. 46 (7) (2020) 573–580.
[69] Y. Liu, H. Su, M. Li, J. Xiang, X. Wu, Y. Zhong, X. Wang, X. Xia, C. Gu, J. Tu, *In situ* formation of a Li_3N-rich interface between lithium and argyrodite solid electrolyte enabled by nitrogen doping, J. Mater. Chem. A 9 (23) (2021) 13531–13539.
[70] Z. Shadike, H. Lee, O. Borodin, X. Cao, X. Fan, X. Wang, R. Lin, S.-M. Bak, S. Ghose, K. Xu, C. Wang, J. Liu, J. Xiao, X.-Q. Yang, E. Hu, Identification of LiH and nanocrystalline LiF in the solidelectrolyte interphase of lithium metal anodes, Nat. Nanotechnol. 16 (5) (2021) 549–554.
[71] H.-L. Wu, R.T. Haasch, B.R. Perdue, C.A. Apblett, A.A. Gewirth, The effect of water-containing electrolyte on lithium-sulfur batteries, J. Power Sources 369 (2017) 50–56.
[72] Z. Wang, D. Santhanagopalan, W. Zhang, F. Wang, H.L. Xin, K. He, J. Li, N. Dudney, Y.S. Meng, In situ STEM-EELS observation of nanoscale interfacial phenomena in all-solid-state batteries, Nano Lett. 16 (6) (2016) 3760–3767.
[73] K. Tomita, H. Noguchi, K. Uosaki, Effect of water on the product distribution at the cathode of Li-O_2 batteries, ECS Meeting Abstracts MA2017–01 (5) (2017), 305–305.
[74] Y. Qiao, S. Wu, J. Yi, Y. Sun, S. Guo, S. Yang, P. He, H. Zhou, From O_2^- to HO_2^-: reducing by-products and overpotential in Li-O_2 batteries by water addition, Angew. Chem. Int. Ed. 56 (18) (2017) 4960–4964.
[75] D. Aurbach, B.D. McCloskey, L.F. Nazar, P.G. Bruce, Advances in understanding mechanisms underpinning lithium-air batteries, Nat. Energy 1 (9) (2016).
[76] H. Durrer, Schillerfarben beim pfau (Pavo cristatus L.), Verhandle. Naturf. Ges. Basel 73 (1962) 204–224.
[77] T.W. Kim, N.-G. Park, Methodologies for structural investigations of organic lead halide perovskites, Mater. Today 38 (2020) 67–83.
[78] V. Kumar, J. Barbé, W.L. Schmidt, K. Tsevas, B. Ozkan, C.M. Handley, C. L. Freeman, D.C. Sinclair, I.M. Reaney, W.C. Tsoi, A. Dunbar, C. Rodenburg, Stoichiometry-dependent local instability in $MAPbI_3$ perovskite materials and devices, J. Mater. Chem. A 6 (46) (2018) 23578–23586.